ELSEVIER

Contents lists available at ScienceDirect

Journal of Non-Crystalline Solids

journal homepage: www.elsevier.com/locate/jnoncrysol





Role of densification in deformation behaviors of model metallic glasses under 3-D nanoindentation studied in molecular dynamics simulation

Haidong Liu^a, Yunfeng Shi^a, Randall E. Youngman^b, Liping Huang^{a,*}

- ^a Department of Materials Science and Engineering, Rensselaer Polytechnic Institute, Troy, NY 12180, USA
- ^b Science and Technology Division, Corning Incorporated, Corning, NY 14831, USA

ARTICLE INFO

Keywords:
Glass
Densification
Shear flow
Crack resistance
Nanoindentation
Classical molecular dynamics simulation

ABSTRACT

Under sharp contact loading, glass deforms elastically and then plastically via densification as well as shear flow. Stress build-up during loading, residual stress build-up after unloading, and possible ultimate cracking all depend sensitively on the competition and interplay between densification and shear flow. The crack resistance was shown in experimental studies to generally improve with the increasing contribution of densification in glasses where shear deformation plays a dominant role under indentation. In this work, the role of densification in deformation behaviors of model metallic glasses under sharp contact loading was studied by 3-D nano-indentation tests using indenters with different sharpness in classical molecular dynamics simulations. Starting from a model metallic glass that favors shear deformation, a Lennard-Jones potential was modified to describe model metallic glasses with different abilities of instantaneous densification under compression and permanent densification after decompression. Our studies show that model metallic glass with a higher densification ability under indentation has less stress build-up and less localized shear deformation during loading, as well as smaller residual stress build-up after unloading. However, our study indicates that both instantaneous and permanent densification need to be tuned for designing damage resistant glasses.

1. Introduction

Although indentation behaviors of glasses have been studied for a very long time, the dependence of deformation modes and cracking patterns on glass composition remains so far to a rough classification between glasses preferentially exhibiting ring/cone cracking (so-called anomalous glasses) and those for which radial-median cracks predominate (so-called normal glasses) [1-4]. A typical anomalous glass, e.g., fused silica, deforms primarily by densification and has a high tendency to form ring/cone cracks that can accompany median/radial and lateral cracks when indented with a Vickers tip. A typical normal glass, e.g., soda-lime silicate glass, mainly deforms by a shearing mechanism and forms median/radial and lateral cracks when indented with a Vickers indenter [5-9]. Previous studies have shown that the crack resistance of glasses exhibiting normal cracking behavior increases as the amount of densification increases [5,10,11]. Sehgal and Ito reported that the crack resistance of glasses that exhibit normal cracking increases as the molar volume increases, which is likely due to the ease of densification for glasses that have more open network structures [12-15]. It was shown that deformation by densification tends to produce less residual stress and less sub-surface damage, so that the threshold load required to initiate cracks increases [16]. However, there should be a limit as a very high level of densification like in silica glass increases the tendency toward ring/cone crack formation [5].

By using a newly developed 3-D nanoindentation method in MD, this study reports a systematic investigation of the role of densification in the deformation behaviors of model metallic glasses under sharp contact loading. Instead of changing compositions, here, we proposed a simple modification to a Lennard-Jones (LJ) potential to tune the densification ability of model metallic glasses under compression and the permanent densification after decompression. Detailed analysis of the stress and strain fields in these model metallic glasses under 3-D nanoindentation provided an atomic level understanding of how densification affects the response of glass favoring shear deformation to sharp contact loading. Our studies show that a higher densification ability under indentation leads to less stress build-up and less localized shear deformation during loading, as well as smaller residual stress build-up after unloading, thus increasing the crack resistance of glass. Insights from this study provide guidelines on how to tune both instantaneous and permanent densification towards damage resistant glasses.

E-mail address: huangL5@rpi.edu (L. Huang).

^{*} Corresponding author.

Table 1BLJ potential parameters.

Sample	Number of bump terms	ε_B	$r_{lphaeta}^{\mathcal{S}}/\sigma_{lphaeta}$	$r_{lphaeta}^E/\sigma_{lphaeta}$
BLJ_0	1	0.8	1.2	1.4
BLJ_1	2	0.8	1.2	1.4
		0.2	1.05	1.10
BLJ 2	2	0.8	1.2	1.4
220_2	-	0.1	1.05	1.11

2. Method

A modified binary Lenard-Jones (BLJ) potential was used to describe atomic interactions in the model glasses [17]. The model BLJ glasses consist of an equal amount of large and small atoms with $m_L=2m_0$, $m_S=m_0$. The $\varepsilon_{\alpha\beta}$ and $\sigma_{\alpha\beta}$ are the energy and length scales of the pair interactions. All bonds have the same strength but different lengths: $\varepsilon_{LL}=\varepsilon_{LS}=\varepsilon_{SS};\ \sigma_{SS}=\left(\frac{5}{6}\right)\sigma_{LL},\ \sigma_{LS}=\left(\frac{11}{12}\right)\sigma_{LL}$. The LJ units are related to the real units as follow: $\sigma_{LL}=2.7\ \text{Å};\ m_0=46\ \text{amu};\ \varepsilon_{LL}=0.151\ \text{eV};\ t_0=0.5\ \text{ps}.$ The functional forms of the BLJ potential are as follows:

$$\varphi_{BLJ}(r) = \varphi_{LJ}(r) + \sum_{i} \varphi_{B,i}(r)$$

$$arphi_{LJ}(r) = 4arepsilon_{aeta} \left(rac{\sigma_{aeta}^{12}}{r^{12}} - rac{\sigma_{aeta}^{6}}{r^{6}}
ight) - 4arepsilon_{aeta} \left(rac{\sigma_{aeta}^{12}}{r_{aeta}^{C}} - rac{\sigma_{aeta}^{6}}{r_{aeta}^{C}}
ight)$$

$$arphi_{B}(r) = egin{cases} 0, & r < r_{aeta}^{S} \ arepsilon_{B} arepsilon_{aeta} \sin^{2} \left(\pi rac{r_{aeta}^{E} - r}{r_{aeta}^{E} - r_{aeta}^{S}}
ight), & r_{aeta}^{E} > r \geq r_{aeta}^{S} \ 0, & r \geq r_{aeta}^{E} \end{cases}$$

$$(1)$$

where $r_{\alpha\beta}^{\mathcal{C}}/\sigma_{\alpha\beta}=1.4$. The additional energy penalty $\varphi_B(r)$ is applied only between $r_{\alpha\beta}^{\mathcal{S}}$ and $r_{\alpha\beta}^{\mathcal{E}}$. The original BLJ (BLJ_0) sample features a single bump term, which is identical to our previous study with $\varepsilon_B=0.8$

[18]. Both BLJ_1 and BLJ_2 have two bump terms, with potential parameters listed in Table 1. Note that the secondary bumps were placed on the repulsive side of the pair-wise interaction in Fig. 1(a) to accommodate the volumetric change under compression, thus giving the system ability to densify. Parameters for BLJ_1 and BLJ_2 are chosen so that the pair interaction is identical to BLJ_0 in the original potential well, and an additional well is only available under compression.

Glass samples were quenched isochorically from high-temperature liquid from 2105 K to 5 K with a cooling rate of 0.83 K/ps using the Nose–Hover thermostat. The samples were then relaxed at 5 K in the NPT ensemble using the Nose–Hover thermostat and barostat for 2500 ps [19–21]. Each as-quenched sample consists of 80,000 atoms. Velocity Verlet integrator with a timestep of 5 fs was used for all simulations in LAMMPS with the KOKKOS acceleration package [22,23].

Uniaxial tensile tests and hydrostatic compression tests were carried out to characterize the mechanical properties of the samples. The tensile tests were done at a constant strain rate of 1 ns⁻¹, and only the strain range up to 0.06 was used to calculate the Young's modulus. The hydrostatic tests were carried out at a constant rate of 5 MPa/ps during loading and unloading under an NPT ensemble. Volumetric strain up to 0.1 was used to calculating bulk modulus. Stress-strain curves of these samples from uniaxial tension tests are shown in Fig. 1(b), which indicates that BLJ_1 and BLJ_2 become slightly stiffer and have a smaller failure strain than BLJ_0, but all three of the model metallic glasses show a clear brittle fracture under uniaxial tension. As shown in Table 2, the BLJ_1 sample has a much higher bulk modulus and Poisson's ratio than the BLJ_0 and BLJ_2 samples. This is due to the larger height of the second bump in BLJ_1 that makes it harder to compress the system (see Fig. 1(a)). The amount of instantaneous densification at the maximum

Table 2
Elastic moduli of BLJ samples.

Sample	Young's modulus (GPa)	Bulk modulus (GPa)	Shear modulus (GPa)	Poisson's ratio
BLJ_0	118.9	83.0	47.6	0.259
BLJ_1	144.5	135.7	54.6	0.323
BLJ_2	129.0	90.0	51.2	0.261

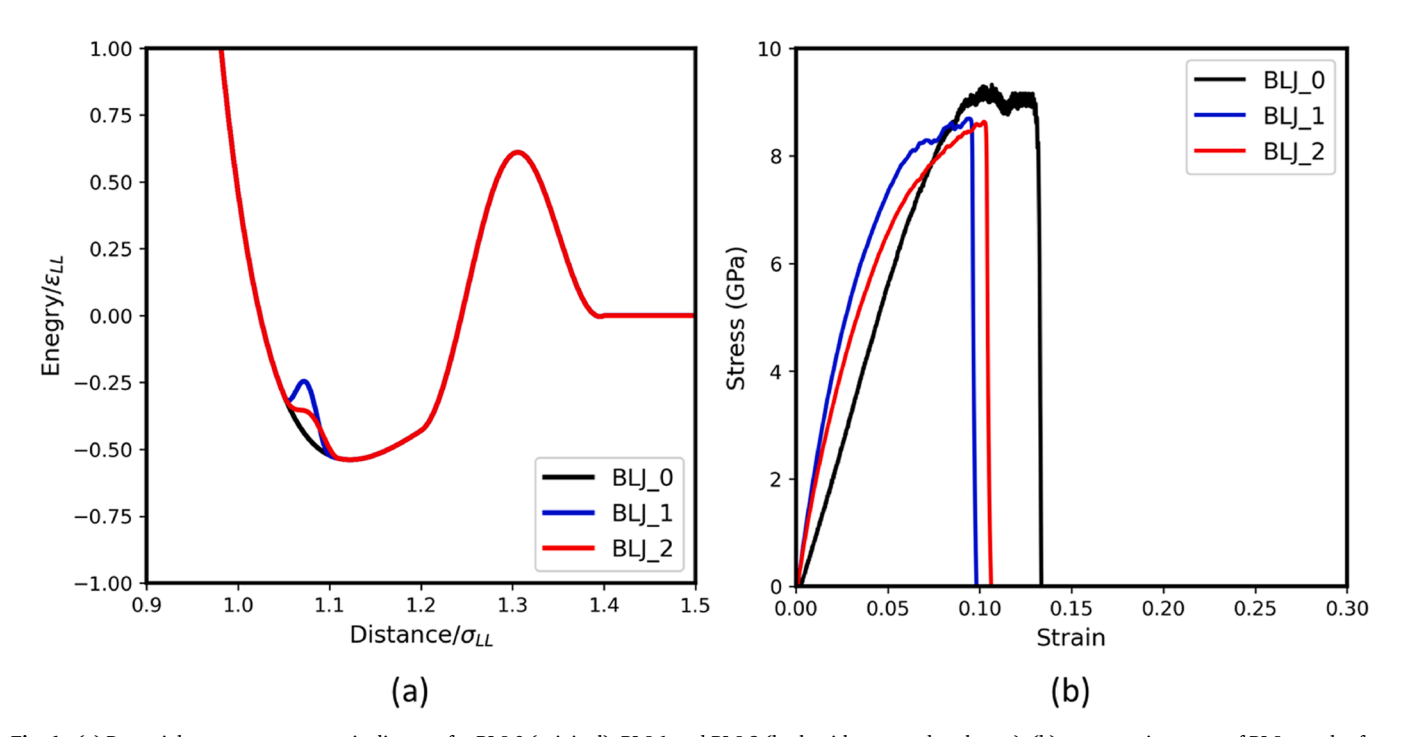


Fig. 1. (a) Potential energy versus atomic distance for BLJ_0 (original), BLJ_1 and BLJ_2 (both with a secondary bump), (b) stress-strain curves of BLJ samples from uniaxial tensile tests.

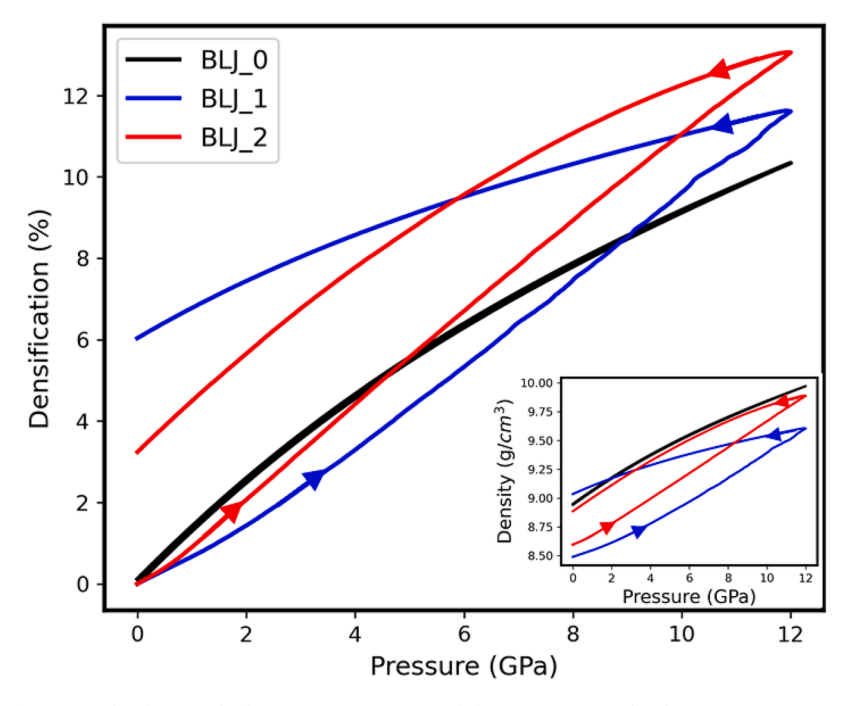


Fig. 2. (a) Densification of BLJ samples during a hydrostatic compression and decompression cycle (density vs. pressure curves are shown in inset).

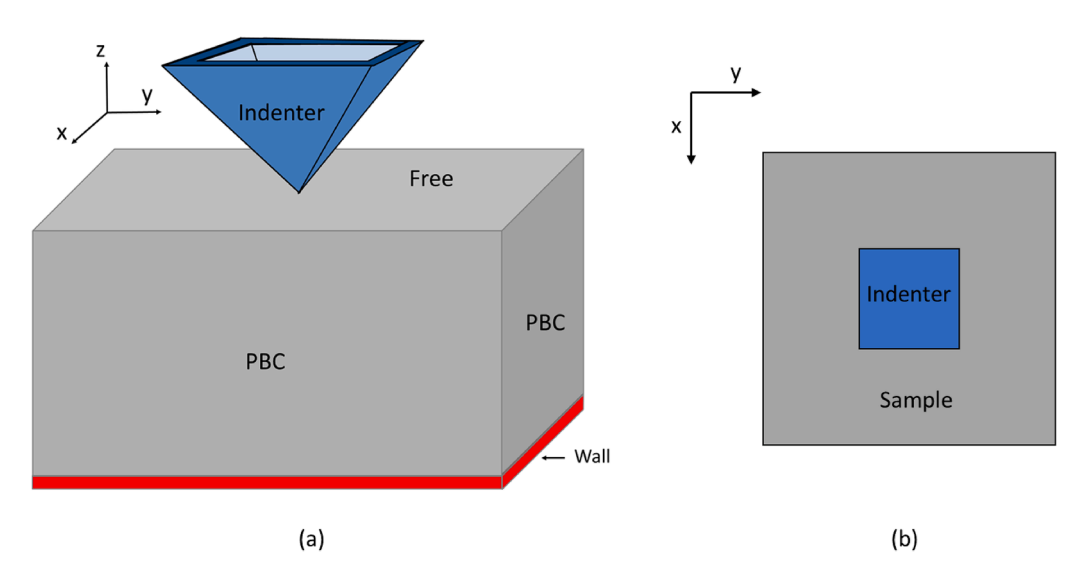


Fig. 3. (a) Side view and (b) top view of the nanoindentation setup in MD simulation.

Table 3Dimensions of samples studied in nanoindentation tests using different indenter angles.

Indenter angle	Dimension <i>x</i> (nm)	Dimension <i>y</i> (nm)	Dimension z (nm)	Total number of atoms
60°	161.5	161.5	218.4	338,800,000
120°	191.7	191.7	153.9	338,800,000

pressure through a hydrostatic compression-decompression cycle determines the naming of samples. As shown in Fig. 2, BLJ_2 has the highest amount of densification at 12 GPa, and BLJ_0 has the lowest.

The as-quenched sample with dimensions of 14.3 nm \times 14.3 nm \times 6.2 nm is replicated in three directions for nanoindentation tests. The schematic of the nanoindentation setup is shown in Fig. 3. Same as in our previous study [18], the indenter has a pyramidal shape similar to the Vickers indenter, characterized by its apex angle and a tip radius of 5

nm. The indenter approaches the sample at a speed of 20 m/s to reach a depth of about 30–50 nm until the sample develops significant plastic deformation. Sample dimensions for indenter angle of 60 and 120° are shown in Table 3, each containing 338,800,000 atoms.

3. Results

Modifying the original BLJ with a secondary bump is intended to tune densification under compression and permanent densification after decompression. As shown in Fig. 2, compared to BLJ_0, the two samples with a secondary bump show enhanced densification at the maximum pressure and more permanent densification after pressure release. BLJ_2 has the highest instantaneous densification at 12 GPa (\sim 13 %), and BLJ_1 has the most permanent densification after decompression (\sim 6 %) although the instantaneous densification at the maximum pressure is lower (\sim 11.5 %). The density of BLJ_0 increases by \sim 10.5 % at 12 GPa, but there is no permanent densification after decompression. The

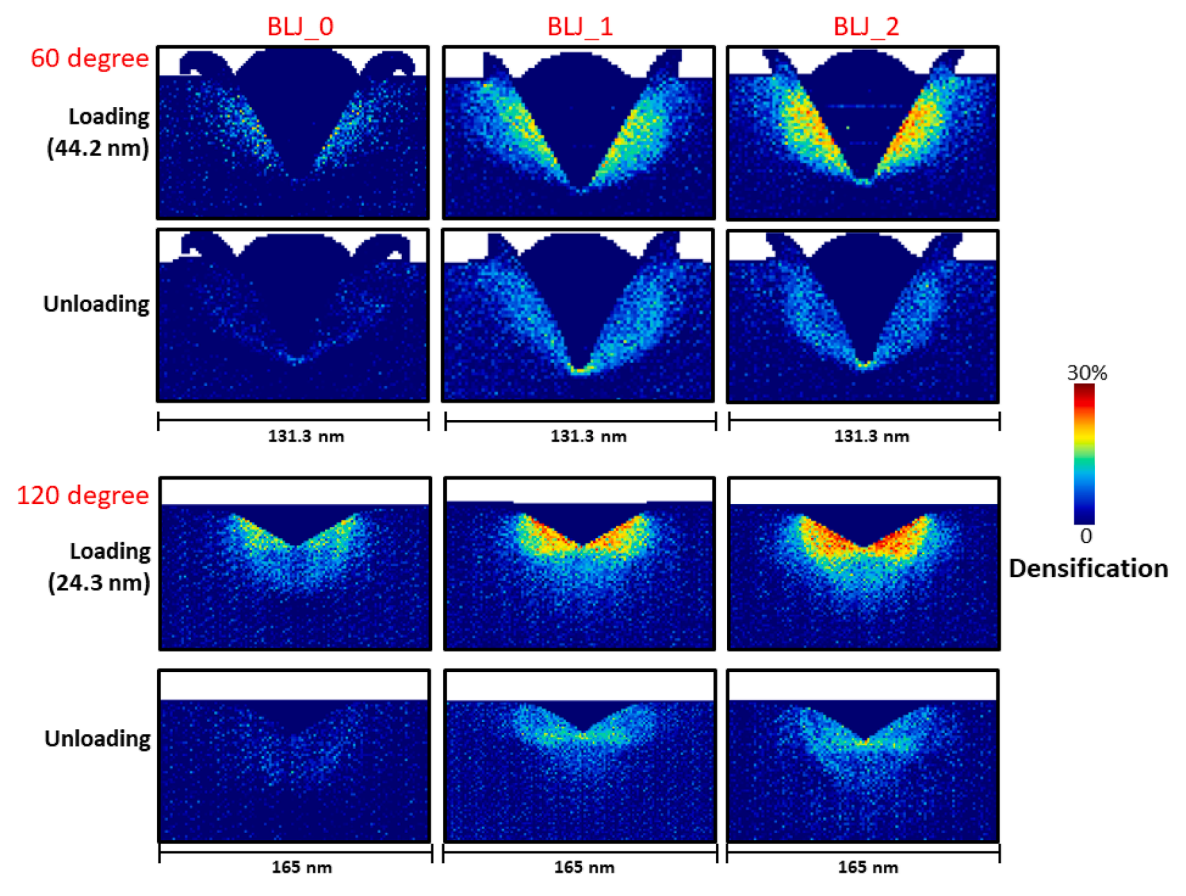


Fig. 4. Densification maps during loading and after unloading from a depth of 44.2~nm and 24.3~nm in 60° and 120° nanoindentation, respectively.

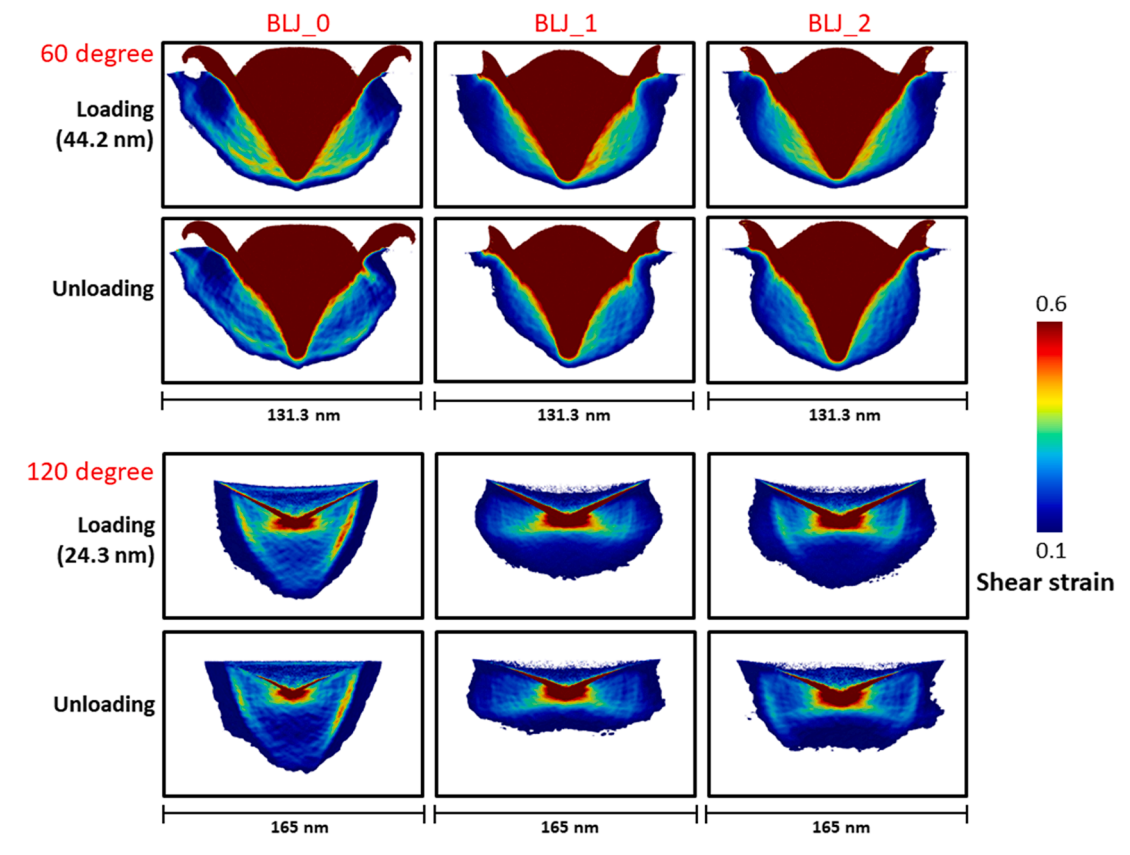


Fig. 5. Atomic shear strain during loading and after unloading from a depth of 44.2 nm and 24.3 nm in 60° and 120° nanoindentation, respectively.

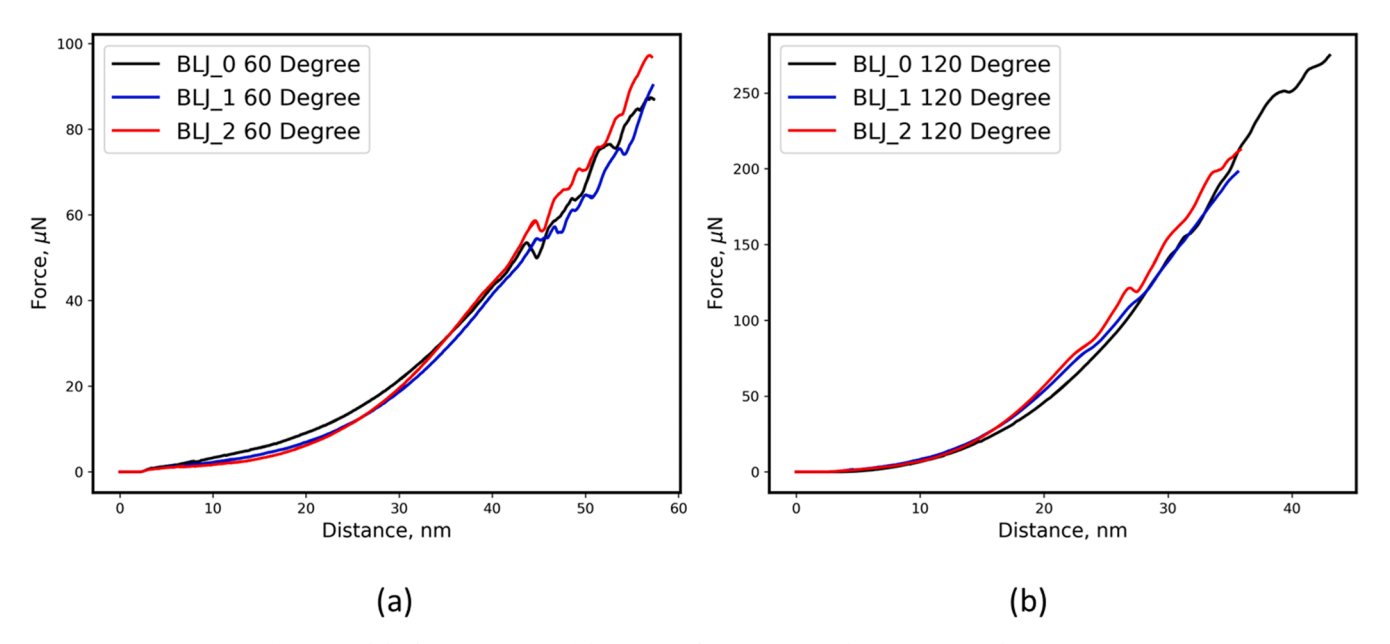


Fig. 6. Load-displacement curves of the BLJ samples in (a) 60° , and (b) 120° nanoindentation tests.

amount of permanent densification in BLJ_1 (\sim 6 %) and BLJ_2 (3.2 %) after decompression from 12 GPa is in the range seen in permanently densified metallic glasses, B₂O₃ glass, and window glasses [24]. It is interesting to note that BLJ_1 has the highest Poisson's ratio (0.323), the lowest permanent densification ability is expected [15,24], yet an opposite trend is seen in Fig. 2. Given the stress field under an indenter is largely compressive, density change during hydrostatic compression and decompression will help us understand the response of glass to

indentation during the loading and unloading process.

Cross-section view of the densification maps under nanoindentation tests along the y axis in the schematics of Fig. 3 are shown in Fig. 4. In 60° and 120° nanoindentation tests, both BLJ_1 and BLJ_2 facilitate more local densification underneath the indenter than BLJ_0. Their densification patterns look similar to a previous study of as-quenched silica glass under indentation, which also has excellent densification ability [25]. Fig. 4 shows that all three samples developed a higher

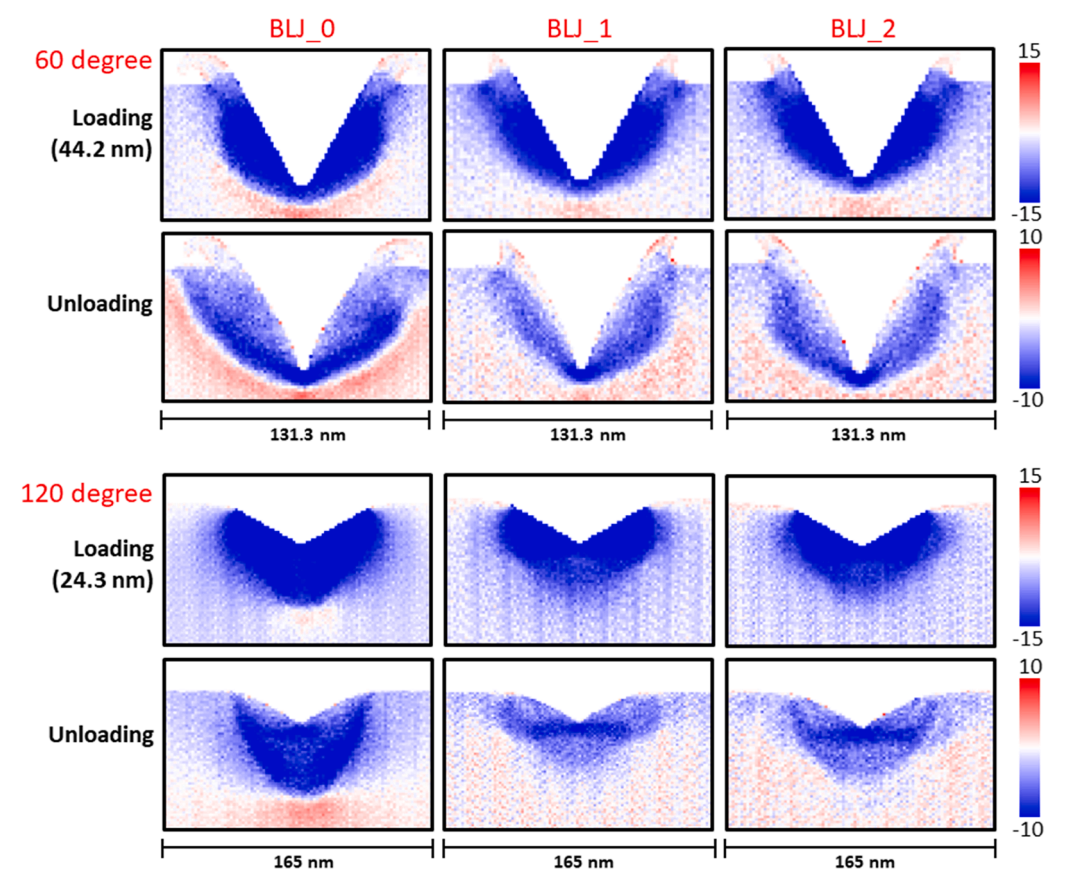


Fig. 7. Maps of I_1 (in the units of GPa) during loading and after unloading from a depth of 44.2 nm and 24.3 nm in 60° and 120° nanoindentation, respectively.

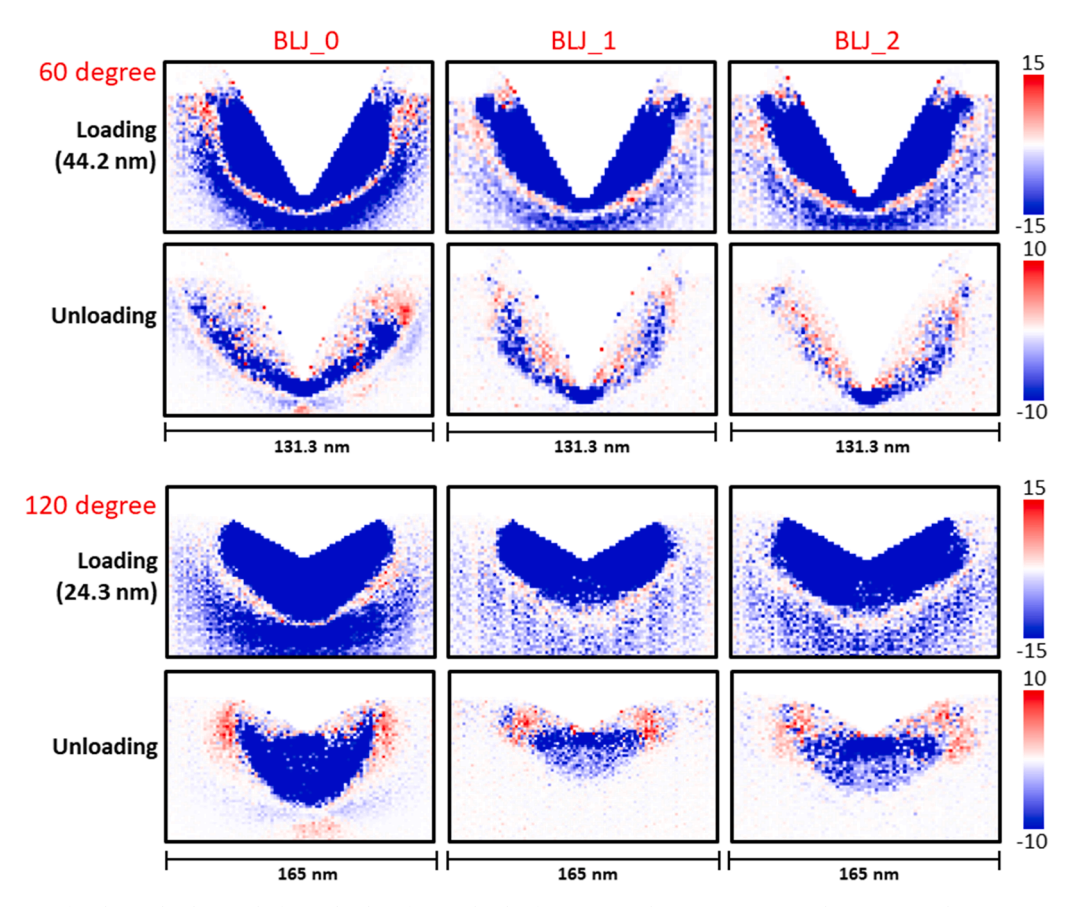


Fig. 8. Maps of I_3 during loading and after unloading from a depth of 44.2 nm and 24.3 nm in 60° and 120° nanoindentation, respectively.

amount of instantaneous densification and permanent densification in 120° indentation than in the 60° nanoindentation test, which agrees with experimental observations that a blunter indenter promotes more densification deformation under indentation [5,26,27]. BLJ_2 shows higher instantaneous densification than BLJ_1 during loading in both 60° and 120° indentation tests, while BLJ_1 shows slightly higher permanent densification near the indenter tip than BLJ_2 after unloading, the difference is more obvious in 60° than 120° indentation test. This difference between BLJ_1 and BLJ_2 is consistent with their instantaneous and permanent densification propensities under compression and after decompression in Fig. 2.

The atomic shear strain under 60° and 120° nanoindentation are analyzed [28,29] and shown in Fig. 5. Our previous study has identified two shear band systems in BLJ_0, namely the upper shear band (USB) and lower shear band (LSB), based on the direction of the shear band propagation relative to the indentation direction [18]. The activation of the shear band is controlled by the indenter angle, in which a sharp indenter with an angle of 60° would activate USB, and a blunt indenter with an angle of 120° would activate LSB. In BLJ_1 and BLJ_2 during loading under both 60° and 120° nanoindentation tests, the shear band activation is suppressed, and the shear deformation is less and takes place more homogeneously than in BLJ_0. Compared to BLJ_0, both BLJ_1 and BLJ_2 exhibit less pile-up under the 60° nanoindentation, and their shear deformation zone size is substantially reduced in the 120° nanoindentation. The shear strain after unloading in Fig. 5 shows that under the 60° nanoindentation, the shear deformation recovers, and the shear deformation zone shrinks for all three samples. On the other hand, under the 120° nanoindentation, the shear deformation reduces slightly, and the shear deformation zone doesn't change appreciably in BLJ 0, while BLJ 1 and BLJ 2 partially recover the shear deformation after unloading, as indicated by the smaller deformation zone. Furthermore, it is very interesting that BLJ_1 shows a better recovery of the shear

deformation than BLJ_0 and BLJ_2 after unloading in both 60° and 120° nanoindentation tests.

The load-displacement curves are shown in Fig. 6 for the three BLJ samples in the 60° and 120° nanoindentation tests. In our previous study, we observed shear band formation correlates with kinks on the load-displacement curve of BLJ_0 [18], which agrees with previous experimental studies where the serrations on the load-displacement curves rise from the shear flow [30,31]. Furthermore, the sharper the indenter, the more pronounced the kinks appear on the load-displacement curves, and at a deeper indentation depth they start to appear [32–35]. Similar trends still hold for the BLJ_1 and BLJ_2 samples. We also observed that the kinks become less evident for the BLJ_1 sample in both 60° and 120° nanoindentation tests. This is consistent with Fig. 5 that BLJ_1 suppresses the formation of the shear band most effectively, as it has a higher shear modulus as seen in Table 2.

In our previous study of BLJ_0, the combination of stress invariants of I_1 and I_3 was used to describe the local stress states [18]. I_1 and I_3 are calculated in Eqs. (2)–(4) below. Eq. (4) represents I_3 using the principle stresses instead of the components of a general stress tensor.

$$I_1 = \sigma_{11} + \sigma_{22} + \sigma_{33} \tag{2}$$

$$I_3 = \sigma_{11}\sigma_{22}\sigma_{33} + 2\sigma_{12}\sigma_{23}\sigma_{31} - \sigma_{12}^2\sigma_{33} - \sigma_{23}^2\sigma_{11} - \sigma_{13}^2\sigma_{22}$$
(3)

$$I_3 = \sigma_1 \sigma_2 \sigma_3 \tag{4}$$

The physical interpretation of I_1 is the local hydrostatic stress state. Our previous study showed that positive I_3 strongly correlates with the shear band activation [18], where the positive region of I_3 in the deformation zone generate most susceptible stress states for shear band activation. Maps of I_1 in Fig. 7 show that in the 60° nanoindentation, BLJ_1 and BLJ_2 have less tensile stress build-up during loading and less

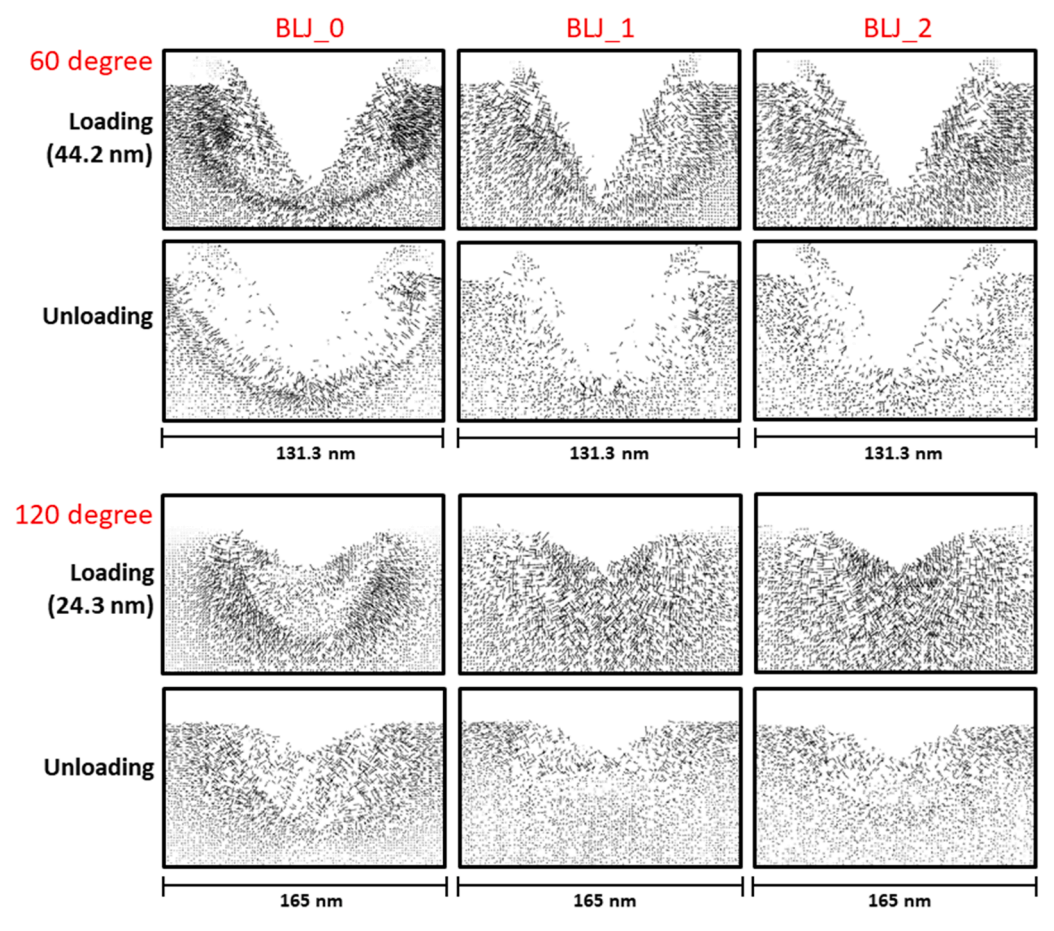


Fig. 9. Patterns of the maximum shear stress r_{13}^{max} (represented by an arrow at each point to indicate the direction and magnitude) during loading and after unloading from a depth of 44.2 nm and 24.3 nm in 60° and 120° nanoindentation, respectively.

residual tensile and compressive stress build-up after unloading than BLJ_0. In the 120° indentation, BLJ_1 and BLJ_2 show less tensile stress and compressive stress build-up during loading and after unloading. Maps of I_3 in Fig. 8 show that a more diffusive band with positive I_3 around the indenter is seen in BLJ_1 and BLJ_2 than in BLJ_0. Both Figs. 7 and 8 show that the BLJ_1 sample has less stress build-up during

loading and less residual stress build-up after unloading than BLJ_2. The difference is more obvious in the 120° nanoindentation than in the 60° nanoindentation.

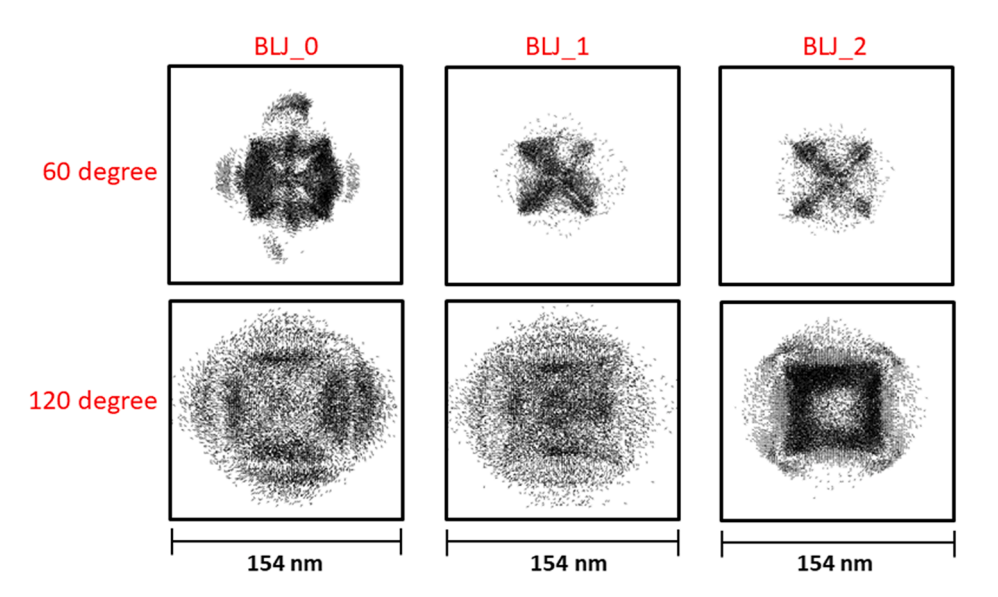


Fig. 10. Patterns of the maximum shear stress τ_{13}^{max} (represented by an arrow at each point to indicate the direction and magnitude) from the top view after unloading from a depth of 44.2 nm and 24.3 nm in 60° and 120° nanoindentation, respectively.

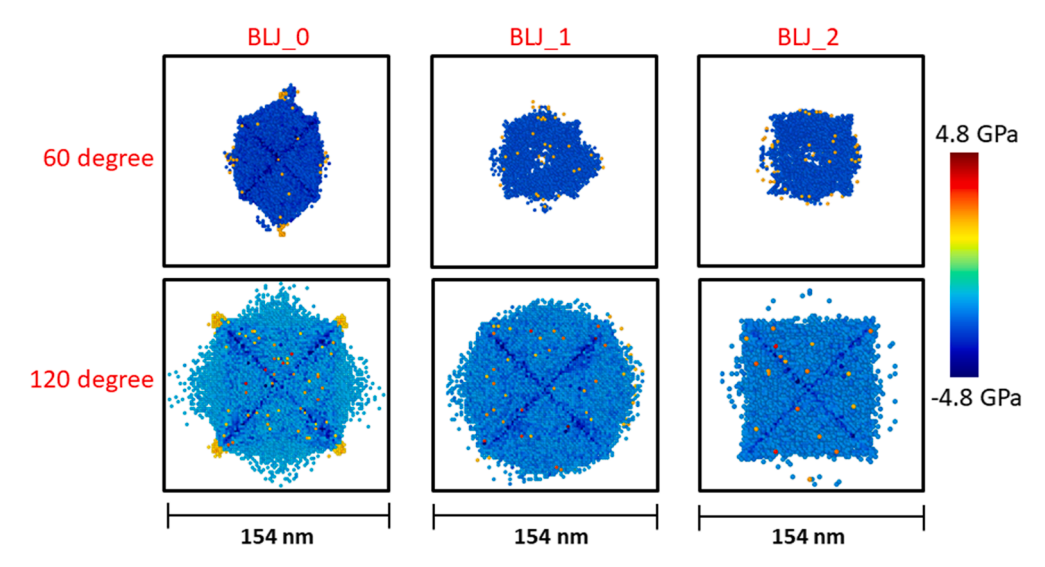


Fig. 11. Patterns of residual hydrostatic stress from the top view after unloading from a depth of 44.2 nm and 24.3 nm in 60° and 120° nanoindentation, respectively.

4. Discussion

Our previous study focused on the shear band activation process to understand the deformation mechanisms in BLJ 0 under indentation [18]. In this study, the role of densification in the response of glass to sharp contact loading was investigated by comparing the three model metallic glasses. As shown in Figs. 4 and 5, BLJ 1 and BLJ 2 facilitate a higher amount of local densification during loading while pinning down the shear bands to introduce more homogenous shear deformation. As shown in our previous study, the shear stress of τ_{13} was found to significantly affect the shear band formation in both 60° to 120° nanoindentation, where the shear bands propagate toward the high-stress region and the shear stress is released after the shear band activation [18]. The maximum shear stress τ_{13}^{max} is defined by the principal stresses, namely the tensile stress σ_1 and the compressive stress σ_3 . For clarity, the top 10 % of the τ_{13}^{max} in 60° and 120° nanoindentation during loading and after unloading are shown in Fig. 9. Unlike BLJ 0, both BLJ 1 and BLJ 2 build up the shear stress homogeneously throughout the deformation zone without significant local accumulation during loading in both 60° and 120° nanoindentation. After unloading, the maximum shear stress of τ_{13} is mostly relaxed in BLJ_1 and BLJ_2, while substantial shear stress remains in BLJ 0. The localization of the shear stress in BLJ 0 is more obvious under the 60° than the 120° nanoindentation during loading and after unloading.

Top view of the residual maximum shear stress τ_{13}^{\max} and the residual hydrostatic stress for these samples are shown in Figs. 10 and 11. After unloading in the 60° nanoindentation, BLJ_1 and BLJ_2 show similar residual stress patterns, but substantially smaller residual stresses than BLJ_0 for both the shear stress in Fig. 10 and the hydrostatic stress in Fig. 11. After unloading in 120° nanoindentation, BLJ_1 has the least residual shear stress, the spatial distribution of the residual shear stress in BLJ 2 is the smallest among the three, but the stress level is higher near the indent as seen in Fig. 10. Fig. 11 shows that BLJ_1 and BLJ_2 have a similar residual hydrostatic stress but smaller than that in BLJ_0. A much higher tensile residual stress accumulates near the indenter corners in BLJ_0, which would promote crack formation during the unloading process [16,36,37]. Fig. 10 also shows that the shape of the residual stress field in BLJ 2 looks quite different from that in BLJ 0 and BLJ_1, more resembling the cross-section of the pyramid indenter than a circular shape seen in the latter two samples.

The above observations show that densification under indentation could enhance the damage resistance of glass by reducing the localized stress build-up during loading and the residual stress build-up after loading, consistent with findings from previous experimental studies [10,16]. Fig. 2 shows that BLJ_1 has less instantaneous densification and more permanent densification than BLJ_2 during a hydrostatic compression-decompression cycle, and it is more effective in reducing the stress build-up during loading, the residual stress build-up after unloading, and in reducing shear localization and relaxing the shear deformation after unloading. The comparison between BLJ_1 and BLJ_2 shows the complicated interaction between shear and densification in affecting the stress and strain fields during the loading and unloading process of indentation. A more detailed study is needed in the future to fine tune the relative contribution of instantaneous and permanent densification to increase the damage resistance of glasses. Between anomalous glasses that primarily deform by densification and normal glasses that mainly deform by a shearing mechanism, intermediate glasses that show deformation behaviors between normal and anomalous seem to hold the promise of having higher crack resistance [5].

5. Conclusions

The role of densification in the deformation behaviors of model metallic glasses was studied using 3-D nanoindentation tests in classical molecular dynamics simulations. A Lennard-Jones potential was modified to allow the system to densify under compression and retain a certain level of permanent densification after decompression. Our studies show that in model metallic glass with a higher contribution of densification under indentation, less stress is built up, less shear deformation is localized during loading, and a smaller residual stress is built up after unloading. However, deformation modes of BLJ 2 under indentation shows that the instantaneous densification under loading may not need to be the higher, the better. Modest instantaneous densification combined with some permanent densification in BLJ_1 indicates that both instantaneous densification and permanent densification need to be tuned to improve the crack resistance of glass. Besides the BLJ system studied in this work, a similar approach could be used in other glass systems to optimize their crack resistance by tuning the densification ability during compression and after decompression.

CRediT authorship contribution statement

Haidong Liu: Writing – review & editing, Writing – original draft, Visualization, Methodology, Investigation. Yunfeng Shi: Writing – review & editing, Writing – original draft, Visualization, Methodology, Investigation. Randall E. Youngman: Writing – review & editing, Writing – original draft, Methodology, Funding acquisition, Conceptualization. Liping Huang: Writing – review & editing, Writing – original

draft, Supervision, Funding acquisition, Conceptualization.

Declaration of competing interest

The authors declare that they have no known competing financial interests or personal relationships that could have appeared to influence the work reported in this paper.

Data availability

Data that support the findings of this study are available from the corresponding author upon request.

Acknowledgment

This work was supported by the National Science Foundation under Grant no. DMR-1508410 and DMR-1936368. Computational Resources from the Center for Computational Innovations (CCI) at RPI were used in performing the simulations.

References

- C.R. Kurkjian, G.W. Kammlott, M.M. Chaudhri, Indentation behavior of soda-lime silica glass, fused silica, and single-crystal quartz at liquid nitrogen temperature, J. Am. Ceram. Soc. 78 (1995) 737–744, https://doi.org/10.1111/j.1151-2916.1995.tb08241.x.
- [2] T. Rouxel, Driving force for indentation cracking in glass: composition, pressure and temperature dependence, Philos. Trans. R. Soc. Math. Phys. Eng. Sci. 373 (2015) 20140140, https://doi.org/10.1098/rsta.2014.0140.
- [3] T. Rouxel, J. Jang, U. Ramamurty, Indentation of glasses, Prog. Mater. Sci. 121 (2021) 100834, https://doi.org/10.1016/j.pmatsci.2021.100834.
- [4] K. Januchta, M.M. Smedskjaer, Indentation deformation in oxide glasses: quantification, structural changes, and relation to cracking, J. Non-Cryst. Solids X 1 (2019) 100007. https://doi.org/10.1016/j.nocx.2018.100007.
- [5] T.M. Gross, Deformation and cracking behavior of glasses indented with diamond tips of various sharpness, J. Non-Cryst. Solids 358 (2012) 3445–3452, https://doi. org/10.1016/j.jnoncrysol.2012.01.052.
- [6] K.W. Peter, Densification and flow phenomena of glass in indentation experiments, J. Non-Cryst. Solids 5 (1970) 103–115, https://doi.org/10.1016/0022-3093(70) 90188-2.
- [7] T. Rouxel, H. Ji, J.P. Guin, F. Augereau, B. Rufflé, Indentation deformation mechanism in glass: densification versus shear flow, J. Appl. Phys. 107 (2010) 094903, https://doi.org/10.1063/1.3407559.
- [8] T. Rouxel, P. Sellappan, F. Célarié, P. Houizot, J.-C. Sanglebœuf, Toward glasses with better indentation cracking resistance, C. R. Méc. 342 (2014) 46–51, https://doi.org/10.1016/j.crme.2013.10.008.
- [9] S. Bruns, T. Uesbeck, S. Fuhrmann, M. Tarragó Aymerich, L. Wondraczek, D. Ligny, K. Durst, Indentation densification of fused silica assessed by Raman spectroscopy and constitutive finite element analysis, J. Am. Ceram. Soc. 103 (2020) 3076–3088, https://doi.org/10.1111/jace.17024.
- [10] Y. Kato, H. Yamazaki, S. Yoshida, J. Matsuoka, Effect of densification on crack initiation under Vickers indentation test, J. Non-Cryst. Solids 356 (2010) 1768–1773, https://doi.org/10.1016/j.jnoncrysol.2010.07.015.
- [11] S. Yoshida, Indentation deformation and cracking in oxide glass-toward understanding of crack nucleation, J. Non-Cryst. Solids X 1 (2019) 100009, https://doi.org/10.1016/j.nocx.2019.100009.
- [12] J. Sehgal, S. Ito, A new low-brittleness glass in the soda-lime-silica glass family, J. Am. Ceram. Soc. 81 (1998) 2485–2488, https://doi.org/10.1111/j.1151-2916.1998.tb02649.x.

- [13] S. Ito, Structural study on mechanical behavior of glass, J. Ceram. Soc. Jpn. 112 (2004) 477–485, https://doi.org/10.2109/jcersj.112.477.
- [14] J. Sehgal, S. Ito, Less-brittle glasses and their mechanical behavior, Rep. Res. Lab. Asahi Glas. 50 (2000) 1–14.
- [15] S. Yoshida, J.-C. Sanglebœuf, T. Rouxel, Quantitative evaluation of indentationinduced densification in glass, J. Mater. Res. 20 (2005) 3404–3412, https://doi. org/10.1557/imr.2005.0418.
- [16] A. Arora, D.B. Marshall, B.R. Lawn, M.V. Swain, Indentation deformation/fracture of normal and anomalous glasses, J. Non-Cryst. Solids 31 (1979) 415–428, https://doi.org/10.1016/0022-3093(79)90154-6.
- [17] Y. Shi, Creating atomic models of brittle glasses for in silico mechanical tests, Int. J. Appl. Glass Sci. 7 (2016) 464–473, https://doi.org/10.1111/ijag.12253.
- [18] H. Liu, Y. Shi, L. Huang, Deformation behaviors of a model metallic glass under 3-D nanoindentation studied in molecular dynamics simulation, J. Non-Cryst. Solids X 16 (2022) 100130, https://doi.org/10.1016/j.nocx.2022.100130.
- [19] S. Nosé, A molecular dynamics method for simulations in the canonical ensemble, Mol. Phys. 52 (1984) 255–268, https://doi.org/10.1080/00268978400101201.
- [20] W.G. Hoover, Canonical dynamics: equilibrium phase-space distributions, Phys. Rev. A 31 (1985) 1695–1697, https://doi.org/10.1103/PhysRevA.31.1695.
- [21] S. Melchionna, G. Ciccotti, B.Lee Holian, Hoover NPT dynamics for systems varying in shape and size, Mol. Phys. 78 (1993) 533–544, https://doi.org/10.1080/ 00268979300100371.
- [22] S. Plimpton, Fast parallel algorithms for short-range molecular dynamics, J. Comput. Phys. 117 (1995) 1–19, https://doi.org/10.1006/jcph.1995.1039.
- [23] H.C. Edwards, C.R. Trott, D. Sunderland, Kokkos: enabling manycore performance portability through polymorphic memory access patterns, J. Parallel Distrib. Comput. 74 (2014) 3202–3216, https://doi.org/10.1016/j.jpdc.2014.07.003.
- [24] T. Rouxel, H. Ji, T. Hammouda, A. Moréac, Poisson's ratio and the densification of glass under high pressure, Phys. Rev. Lett. 100 (2008) 225501, https://doi.org/ 10.1103/PhysRevLett.100.225501.
- [25] F. Yuan, L. Huang, Brittle to ductile transition in densified silica glass, Sci. Rep. 4 (2015) 5035, https://doi.org/10.1038/srep05035.
- [26] S. Yoshida, H. Sawasato, T. Sugawara, Y. Miura, J. Matsuoka, Effects of indenter geometry on indentation-induced densification of soda-lime glass, J. Mater. Res. 25 (2010) 2203–2211, https://doi.org/10.1557/jmr.2010.0287.
- [27] J.F.S. Christensen, N.M.A. Krishnan, M. Bauchy, M.M. Smedskjaer, Indenting glasses with indenters of varying stiffness and sharpness, J. Non-Cryst. Solids 603 (2023) 122111, https://doi.org/10.1016/j.inoncrysol.2022.122111.
- [28] M.L. Falk, J.S. Langer, Dynamics of viscoplastic deformation in amorphous solids, Phys. Rev. E 57 (1998) 7192–7205, https://doi.org/10.1103/PhysRevE.57.7192.
- [29] F. Shimizu, S. Ogata, J. Li, Theory of shear banding in metallic glasses and molecular dynamics calculations, Mater. Trans. 48 (2007) 2923–2927, https://doi. org/10.2320/matertrans.MJ200769.
- [30] L. Anand, C. Su, A theory for amorphous viscoplastic materials undergoing finite deformations, with application to metallic glasses, J. Mech. Phys. Solids 53 (2005) 1362–1396, https://doi.org/10.1016/j.jmps.2004.12.006.
- [31] C.A. Schuh, T.G. Nieh, A survey of instrumented indentation studies on metallic glasses, J. Mater. Res. 19 (2004) 46–57, https://doi.org/10.1557/ imp. 2004.10.1.46
- [32] C.A. Schuh, T.G. Nieh, A nanoindentation study of serrated flow in bulk metallic glasses, Acta Mater. 51 (2003) 87–99, https://doi.org/10.1016/S1359-6454(02) 00303-8.
- [33] L. Krämer, V. Maier-Kiener, Y. Champion, B. Sarac, R. Pippan, Activation volume and energy of bulk metallic glasses determined by nanoindentation, Mater. Des. 155 (2018) 116–124, https://doi.org/10.1016/j.matdes.2018.05.051.
- [34] K.P. Marimuthu, K. Lee, J. Han, F. Rickhey, H. Lee, Nanoindentation of zirconium based bulk metallic glass and its nanomechanical properties, J. Mater. Res. Technol. 9 (2020) 104–114, https://doi.org/10.1016/j.jmrt.2019.10.034.
- [35] B.-G. Yoo, J.-Y. Kim, J. Jang, Influence of indenter geometry on the deformation behavior of $Zr_{60}Cu_{30}Al_{10}$ bulk metallic glass during nanoindentation, Mater. Trans. 48 (2007) 1765–1769, https://doi.org/10.2320/matertrans.MJ200752.
- [36] A.G. Evans, T.R. Wilshaw, Quasi-static solid particle damage in brittle solids—I. Observations analysis and implications, Acta Metall. 24 (1976) 939–956, https://doi.org/10.1016/0001-6160(76)90042-0.
- [37] R.F. Cook, G.M. Pharr, Direct observation and analysis of indentation cracking in glasses and ceramics, J. Am. Ceram. Soc. 73 (1990) 787–817, https://doi.org/ 10.1111/j.1151-2916.1990.tb05119.x.